Matter

CellPress

Article

Swelling of a non-vascular-plant-inspired soft composite

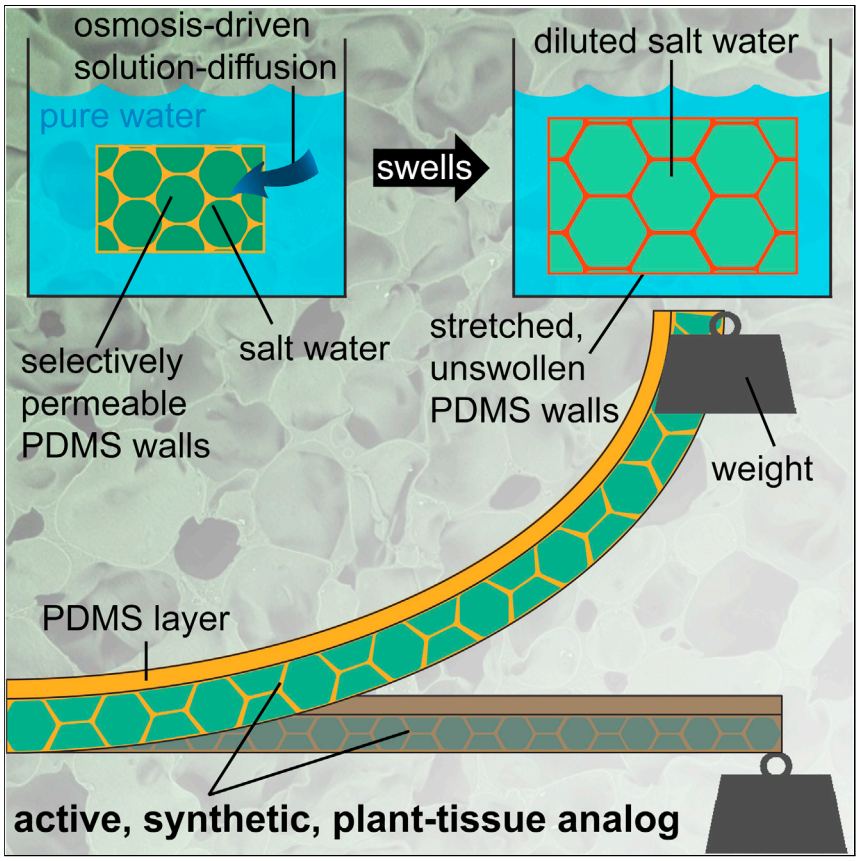

Like plant tissue, closed-cell, fluid-filled silicone + saltwater composites are shown to exhibit large, forceful motion. These materials are created via an emulsion templating process, producing a microstructure that closely resembles non-vascular plant tissue. Saltwater contained within thin silicone walls draws water into the composite. Upon swelling, the walls stretch, producing a turgor pressure inside the pores that eventually counterbalances this osmotic flow, leading to equilibrium. Similar to plants, these materials stiffen with increasing hydration, leading to forceful movements.

Amrita Kataruka, Shelby B. Hutchens

hutchs@illinois.edu

Highlights

Plant inspired silicone + saltwater composites exhibit an osmotically active response

Swelling balances osmotic pressure with turgor pressure from stretched silicone walls

Swollen composites stiffen, rather than soften, leading to higher force actuation

4 **Demonstrate**
Proof-of-concept of performance with intended application/response

Kataruka & Hutchens, Matter 4, 3991–4005
December 1, 2021
https://doi.org/10.1016/j.matt.2021.10.015

Matter

CellPress

Article

Swelling of a non-vascular-plant-inspired soft composite

Amrita Kataruka[1] and Shelby B. Hutchens[2,3,4,*]

SUMMARY

Even without the aid of muscle, plant tissue drives large, forceful motion via osmosis-driven fluid flow. Hydrogels are well-known synthetic materials that mimic this osmotic mechanism to achieve large swelling deformations. However, hydrogels can be limited by a loss of stiffness as their swelling increases. Here we demonstrate that a synthetic plant tissue analog (PTA) can mimic the closed-cell structure and osmotic actuation of non-vascular plant tissue, enabling the emergence of turgor-pressure-induced stiffness and leading to more forceful swelling deformations. PTAs consist of micrometer-sized saltwater droplets embedded within thin, highly stretchable, selectively permeable polydimethylsiloxane (PDMS) walls. When immersed in water, PTAs reach a state of equilibrium governed by the initial osmolyte concentration (higher produces more swelling) and cell wall mechanical response (stiffer and less stretchable yields less swelling). Given these behaviors, PTAs represent an alternate class of aqueous, autonomous synthetic materials that, like hydrogels, may benefit biomedical applications.

INTRODUCTION

Plant tissues achieve striking, forceful movement driven by fluid flow rather than muscle.[1–4] Often it is the tissue's ability to maintain an internal hydrostatic pressure above atmospheric levels, also known as turgor pressure, that enables the strength of these motions. By these means, plants resist gravity, penetrate soil, and overcome energetic barriers to leverage instability.[5] Maintaining turgor pressure at equilibrium requires closed cells to encapsulate the fluid (Figures 1A and 1B). Because these encapsulating cell walls are solid, flow must occur via solution into and then diffusion through the wall material[6–10] (Figure 1C) rather than proceeding via open pores between chambers as in typical poroelastic solids.[11,12] Positive turgor pressure in the tissue relative to the environment creates a driving force for fluid to leave the tissue, leading to shrinkage. In contrast, osmotic pressure differences between the cell cavities and surrounding fluid draw fluid in, leading to swelling-induced deformation.

These plant-like features and functions have inspired innumerable device and material mimics.[14–22] Hydrogels in particular are a well-known class of synthetic materials whose equilibrium swelling shares several features of this chemical-energy-driven mechanism. As such, they provide a useful reference against which to compare the swelling behavior of the plant tissue analogs (PTAs) described here. Similarities between hydrogels and PTAs include their high water content, generally > 80% water by volume; internal chemical energy supply; and self-driven deformation in aqueous environments. These features have contributed to extensive recent interest

Progress and potential

Synthetic hydrated materials share their characteristic stiffness and composition with biological tissues, which makes them promising biomaterial candidates. Their usefulness is further enhanced by their ability to actuate and mechanically respond to environmental stimuli. However, typical hydrated materials (hydrogels) lack the ability to apply forces large enough to support or functionally load tissues and organs. Inspired by plants' ability to structurally support and move themselves using osmosis-driven water pressure, the synthetic plant tissue analogs demonstrated here represent a new class of hydrated soft material capable of forceful, active motion. An encapsulated osmolyte means the material requires no external power source for operation, only a hydrated environment.

in hydrogel materials as autonomous valves,[23] soft robots,[24] and mechanically active wound dressings,[25] to name a few examples. Although such hydrogels have been made mechanically robust through recent double-network approaches,[26,27] there remains a fundamental shortcoming inherent to their operation. Their modulus decreases, i.e., they soften, upon swelling due to the accompanying decrease in cross-link density as the polymer network expands to accommodate volume change.[28–30] This feature limits hydrogel use when deformation is resisted by high force. In contrast, we demonstrate here that, like non-vascular plant tissue, PTAs can maintain, or in some cases increase, their stiffness, thereby outperforming a similar-modulus hydrogel in two proof-of-concept actuation scenarios, illustrated schematically in Figure 1D. The nature of fluid flow within hydrogels versus PTAs further differentiates these materials. Hydrogels have an open network for fluid flow, and thus their swelling dynamics and chemo-mechanical response have been well described by classic poroelasticity approaches.[31–34] Conversely, PTAs' absence of pore-mediated flow makes Darcy's law unphysical. Questions pertaining to the response dynamics associated with these coupled fluid-solid interactions remain open and will be addressed in future work. The current study focuses on the equilibrium swelling response of these new materials to demonstrate that (1) the basic mechanism of turgor pressure-mediated swelling equilibrium is supported by experimental observation, and (2) PTAs can match, and in some ways exceed, the actuation capabilities typical of hydrogels.

Osmotically active structures comprising an osmotic solution, semi-permeable membrane, and deformable surface have previously been reported in the literature.[20,35–39] However, these structures fall short of true PTAs in two important ways. First, the selectively permeable membrane that mediates fluid transport is rigid, necessitating two active surfaces, one for transport and the other for deformation.[20,35–39] Second, previous assembly approaches have isolated the osmotic chambers from one another. The absence of membrane multifunctionality and focus on a single compartmental response means that these efforts are better classified as devices or structures rather than materials, as more accurately describes the PTAs presented here. As materials, PTAs can be readily molded into unique geometries (Supplemental information; Figure S8) and may eventually be described by multi-physics constitutive models. Finally, although such osmotic actuation has been critiqued as being unidirectional, recently, Must et al. demonstrated that an osmotic driving force can be reversed through the electrosorption of ions.[39] These advances may mean that actuation can be reversed for future iterations of PTAs. The results presented here thus lay the groundwork for understanding the behavior of this new class of active material.

Like plant tissue, inter-cavity fluid transport governs the operation of these multi-"cellular" materials. This plant-like response is not possible without a fabrication technique that yields closed pores with thin, selectively permeable walls *and* a readily varied inner phase. We recently developed a method to achieve these features through an emulsion templating process resulting in tightly packed, aqueous-filled, microcavity inclusions (>80% volume fraction) in an elastomeric matrix.[40] We use silicone for the elastomeric matrix due to its inherent combination of highly stretchable and selectively permeable properties. Until recently, such closed-cell structures with high aqueous volume fraction were not possible with silicone due to the prohibitively large difference in viscosity between the two phases that limited traditional emulsification approaches. Our three-step approach of (1) creation of a low-volume-fraction Pickering emulsion, (2) centrifugation to a high-volume-fraction emulsion, and (3) fractionation to eliminate cavity size gradients produces a

[1]Department of Civil and Environmental Engineering, University of Illinois Urbana-Champaign, Urbana, IL 61801, USA

[2]Department of Mechanical Science and Engineering, University of Illinois Urbana-Champaign, Urbana, IL 61801, USA

[3]Department of Material Science and Engineering, University of Illinois Urbana-Champaign, Urbana, IL 61801, USA

[4]Lead contact

*Correspondence: hutchs@illinois.edu

https://doi.org/10.1016/j.matt.2021.10.015

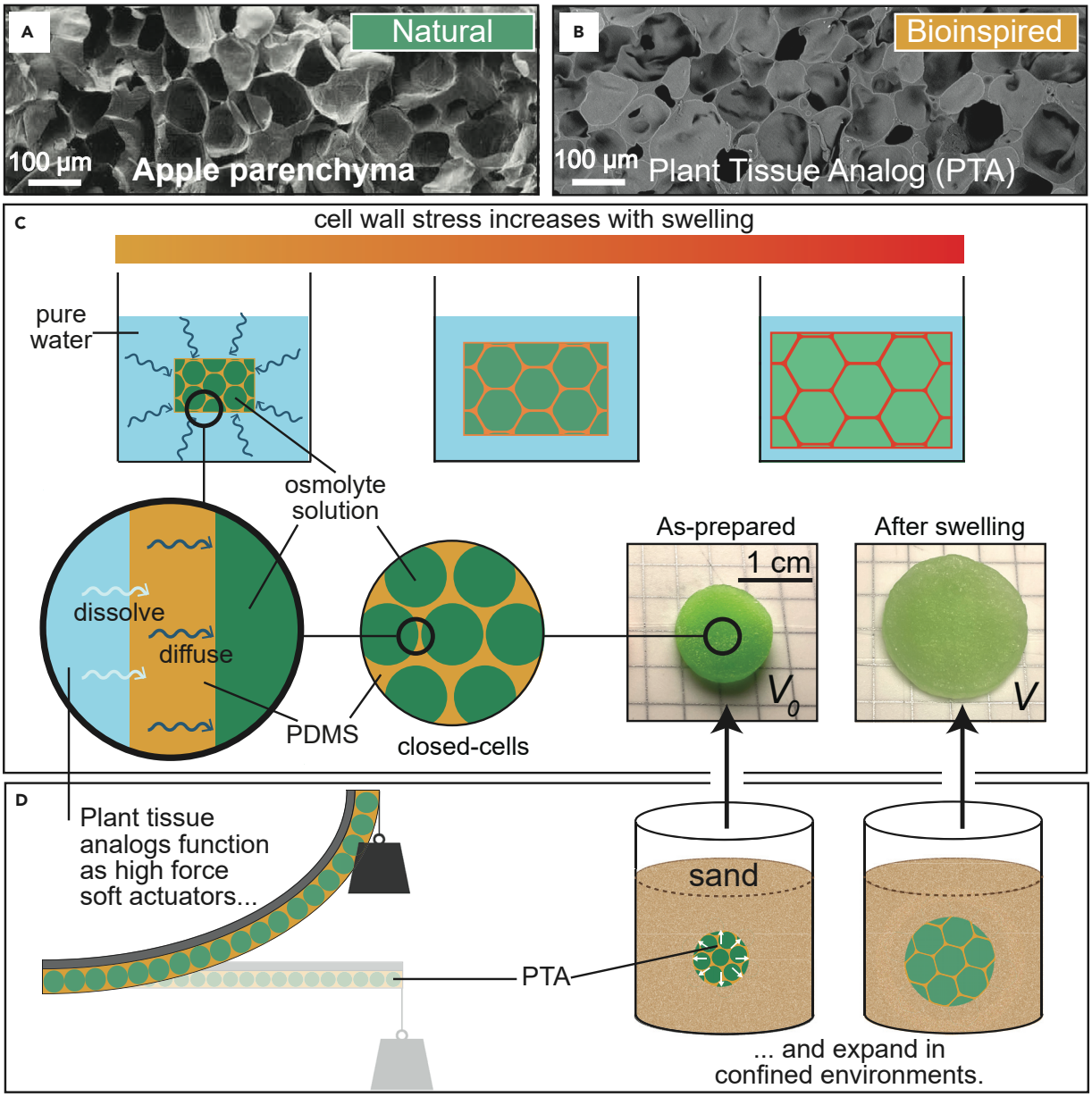

Figure 1. Overview

(A) A scanning electron micrograph (SEM) image of dried plant parenchyma (apple tissue) showing densely packed, closed-cell cavities about 100 µm in size, reproduced with permission.[13]

(B) An SEM image of the cross section of a representative, dried PTA having analogous structure.

(C) Fluid transport in PTAs occurs by dissolving into and then diffusing through the selectively permeable PDMS membrane (orange). The periodic image in the center shows a cross section through seven nominally spherical, osmolyte-filled cavities. The PTAs swell when water flows into these cavities, stretching the cell walls and increasing the stress in them. The digital images show typical as-prepared (left) and swollen (right) PTAs.

(D) Schematics demonstrating how PTAs can behave as a high-force soft actuator by lifting a weight or displacing sand.

composite meso-structure that closely resembles the structure of plant parenchyma tissue (Figures 1A and 1B).[40] Within the cavities, a readily tunable NaCl concentration serves as an osmolyte to establish an osmotic driving force between the PTA and an external water bath (Figure 1C).

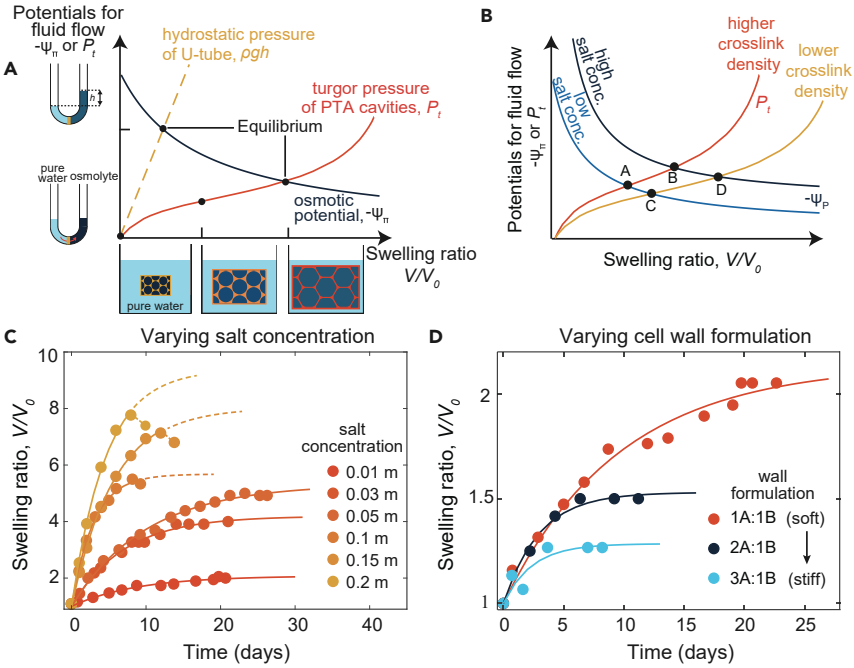

Figure 2. Equilibrium swelling

(A) Osmotic potential drives water into cavities, while infinite flow is resisted by the emergence of hydrostatic pressure. The graph illustrates the interplay of these energetic potentials for fluid flow: osmotic (dark blue solid line) and hydrostatic (light orange dashed and orange solid lines), as the volume of the osmolyte phase increases. Traditional U-tube experiment: hydrostatic pressure is linear due to the pull of gravity on the difference in height between the pure and osmolyte phases as shown by schematics on the y axis. PTAs: turgor pressure (P_t) is nonlinear due to material nonlinearity accompanying the increase in wall stress for expanding cells as shown by schematics along the x axis.

(B) A schematic illustrating the effect of initial salt concentration and crosslink density on equilibrium swelling volume, indicated by the intersection of blue and orange lines. Blue lines of increasing saturation denote osmotic potential for increasing initial salt concentration. The orange lines of increasing saturation represent turgor pressure for increasing crosslinker (higher modulus, less stretchability).

(C) The swelling response of PTAs using a constant PDMS formulation (1A:1B) and varying initial salt concentration. Points and lines correspond to experimental data and exponential fits, respectively. PTAs with lower salt concentrations reach equilibrium (solid lines), while higher salt concentrations rupture (dashed lines).

(D) The swelling response of PTAs having constant initial salt concentration (0.01 m) and varying PDMS formulation. Equilibrium swelling is inversely related to the amount of crosslinker in the PDMS.

As shown by the results to follow, these elastomeric fluid-solid composites behave as non-vascular plant tissue. The osmotic pressure differential established by the NaCl drives water into the cells, stretching the cell walls and giving rise to turgor pressure, P_t (Figures 1C and 2A). P_t provides a potential for counter-flow, eventually bringing the material into equilibrium. Consequent changes in cell structure and wall stiffness increase the stiffness of these fluid-filled, closed-cell composites. Later, we present proof-of-concept demonstrations that this stiffness increase enhances PTA actuation capabilities (Figure 1C). That is, they demonstrate dramatic hydrogel-like swelling but with improved force application.

RESULTS AND DISCUSSION

Swelling response

As Figure 2A illustrates, equilibrium swelling is associated with a balance between the osmotic driving force provided by the salt and the opposing pressure associated

Table 1. Comparison of PDMS constitutive parameters

	Tensile fit elastomer only		Swelling fit elastomer + nanoparticles		Composite estimate elastomer + nanoparticles
Formulation ratio (A:B)	E_{PDMS} (kPa)	J_{lim}	E_w(kPa)	J_{lim}	$\tilde{E}_w$ (kPa)
1:1	291.2	15.98	929.31	5.96	641
2:1	606.7	7.45	1,481.5	3.49	1,335
3:1	816.8	5.08	1,753.1	2.59	1,797

with the stretching PDMS walls. Note the nonlinear response arising from the elastomer wall (dark orange curve), which contrasts with the classic example of a U tube with a selectively permeable membrane barrier (light orange dashed line). In both scenarios, water potential Ψ quantifies the energetic potential that leads to fluid flow.[41] Like a chemical potential difference, water potential quantifies the free energy of a substance relative to a reference state. For water potential, the reference is always pure water, in this case at atmospheric conditions. Water potential has units of pressure and is thus convenient to use for the current system as its mechanical contribution is simply the hydrostatic pressure (P_t for the PTAs, ρgh for the U-tube) and the presence of solute is captured via the osmotic potential Ψ_Π. The summation of these potentials for fluid flow lead to an expression for the water potential within the cavity,

$$\Psi_{PTA} = \Psi_\Pi + P_t, \qquad \text{(Equation 1)}$$

which, when combined with the potential of the surroundings, determines if fluid is driven into or out of a cavity. Here, $\Psi_\Pi = -iCRT$ and i, C, R, and T and are the solute dissociation factor, solute concentration, universal gas constant, and temperature, respectively. Equilibrium occurs when the potential difference between the cells and the water bath vanishes, $\Psi_{PTA} - \Psi_{bath} = 0$. We use a deionized bath at atmospheric conditions, thus $\Psi_{bath} = 0$ and, under our experimental conditions, $\Psi_{PTA} = 0$ at equilibrium. (This equilibrium condition is the same as the chemical potential equilibrium, ESI.) Figure 2A illustrates the balance of the components of this potential driving fluid flow by plotting $-\Psi_\Pi$ and P_t versus the degree of swelling. For the initial salt concentration at zero deformation, $\Psi_{PTA} < 0$ since $P_t = 0$. As water moves into the cavities, the solution dilutes, making Ψ_Π less negative. The simultaneous increase in cavity volume stretches the walls, increasing P_t. Equilibrium occurs at the intersection of the osmotic $-\Psi_\Pi$ and turgor P_t curves. As Figure 2B shows, higher crosslink density yields a stiffer, less stretchable PDMS (Table 1), which increases the material's resistance to swelling. Lower initial salt concentration C_0 reduces the driving force for swelling (blue curves). The highest swelling occurs for walls with less crosslinker enclosing a higher salt concentration (point D).

To validate this description of the anticipated behavior, we incubate PTAs comprising three PDMS formulations of varying crosslinker in deionized water (Table 2). Their cavities are filled with salt concentrations ranging from 0.01 to 0.2 m. (The unit m denotes molality, defined as the number of moles of solute per mass [in kilograms] of solvent.) As Figure 2C shows, swelling throughout the time-dependent response, denoted as the ratio of the sample volume over the initial sample volume V/V_0, decreases with decreasing salt concentration. The time dependence is captured by an exponential saturation curve ($V_{eq}/V_0[1 - e^{-t/\tau}]$) (solid lines). At lower salt concentrations, an equilibrium value V_{eq}/V_0 is reached. For the highest salt concentrations, the swelling reaches a critical value before abruptly decreasing. We interpret this apparent deswelling as the loss of water accompanying rupture of

Table 2. PTA fabrication parameters

Formulation ratio (A:B)	Hexane (wt %)	Mixing speed (rpm)	Pre-fractionation centrifugal force (× *g*)	Post-fractionation centrifugal force (× *g*)
1:1	20	600	3,000; 15 min	3,000; 30 min
2:1	20	600	2,900; 15 min	3,000; 40 min
3:1	23	700	2,400; 8 min	3,000; 20 min
1:1 (5% glycerol)	20	600	2,500; 10 min	3,000; 20 min
1:1 (33% glycerol)	20	600	1,300; 15 min	3,000; 7 min

the thin cavity walls due to excessive stretching as visual observation suggests a loss of sample integrity (ESI; Figure S2). Such rupture resembles plasmoptysis in plants.[42] Salt leakage appears to be minimal over the timescale of these experiments. These data also show that a larger initial salt concentration corresponds to a greater initial water potential difference, increasing the driving force for fluid influx. As a result, we observe an increase in the initial slope as a function of increasing concentration. Analogously, the initial rate of swelling is unaffected by the wall mechanical response when the initial salt concentration is the same, as shown in Figure 2D. The latter swelling curves follow the same trajectory until the wall material's stiffness and finite stretchability take over the response, leading to equilibrium. As predicted in Figure 2B, given the same initial salt concentration, PTAs with higher crosslinker density swell less.

A simple, quantitative model captures the equilibrium swelling for PTAs. It also enables the extraction of wall material properties, via fitting, which are critical when comparing stiffening observations with composite modulus theories. Inspired by previous treatments of plant tissue,[43–45] we model the PTA composite structure as an inflating balloon.[46] The spherical shell is filled with an incompressible fluid having an initial water potential dictated by the salt concentration. For an infinitely thin and stretchable shell wall, the salt concentration would be solely responsible for equilibrium swelling and equilibrium, $\Psi_{PTA} - \Psi_{bath} = 0$, would only be possible when water influx is infinite. We estimate the magnitude of the turgor pressure P_t counteracting this limit by treating the wall material as incompressible and hyperelastic.[46,47] The response of a single, cell-sized sphere is identical to a collection of non-interacting cell-sized spheres, which approximate the composite structure of the PTAs. Since the wall is incompressible, selectively permeable, and does not swell, an increase in volume decreases the osmotic potential Π according to $\Pi V = \Pi_0 V_0$, where Π_0 is the initial osmotic potential $iC_0RT = -\Psi_{\Pi,0}$. Simultaneously, P_t is given by the inflation of a nonlinear elastic balloon of finite wall thickness assuming a strain-stiffening, Gent material model (ESI).[46] At lower stretches, the Gent material model recovers a neo-Hookean response having Young's modulus E. At larger stretches, the model strain stiffens due to a finite stretch limit governed by the limiting stretch parameter J_{lim} (ESI) (in this geometry, $J_{lim} = 5$ corresponds to infinite turgor pressure at $V/V_0 \approx 8$). Thus, for a given PTA geometry, osmotic potential, and wall material, the model estimates the equilibrium expansion ratio; i.e., when $\Psi_{PTA} = 0$.

We capture the equilibrium response of the PTAs as illustrated by the solid curves in Figure 3A using two fit parameters governing the wall material response, E_w and J_{lim}. The data we fit (squares) correspond to the equilibrium volume expansion ratio of the PTAs as estimated from exponential fits of the time-dependent swelling data in Figure 2. Dashed lines describe the decrease in osmotic potential of the samples as they swell. A neo-Hookean response (dotted lines) fails to capture the arrested swelling observed at higher osmotic potential. Rather, describing the PTA's equilibrium response requires both strain stiffening and large deformation behavior for the wall material.

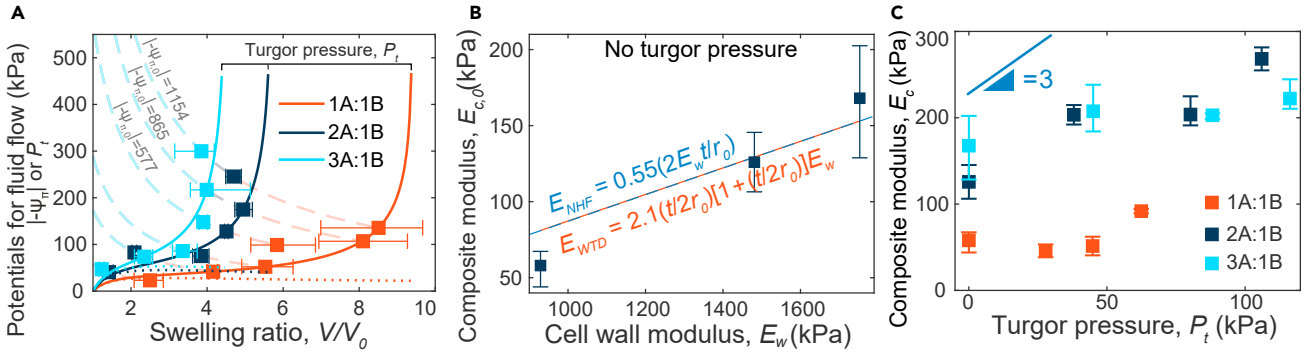

Figure 3. Modeling equilibrium swelling

(A) Experimental equilibrium volume expansion ratio V_{eq}/V_0 of PTAs with varying initial salt loads (squares) and matrix formulation (colors). Position on the y axis is determined by the intersection of the $|\Psi_{\Pi,0}|$ curve (dashed lines) for the C_0 used and the corresponding V_{eq}/V_0. Solid and dotted lines represent the turgor pressure of Gent and neo-Hookean constitutive models, respectively.

(B) The composite Young's modulus of PTAs at zero turgor pressure as a function of cell wall modulus. Fit lines for Warner et al.'s[48] and Nilsson et al.'s[49] predictions use wall thickness and cell sizes of t = 4 μm and r_0 = 50 μm, respectively.

(C) The composite Young's modulus of swollen PTAs as a function of turgor pressure. Modulus is maintained or slightly increases with turgor pressure. The line at the top provides the dependence predicted by Nilsson et al. for comparison.

The cavity wall is composed of both PDMS and a high concentration of silica nanoparticles, which act as the emulsion stabilizer during sample fabrication. Thus, material properties obtained via the swelling model differ from those determined from fitting tensile test data on pure PDMS of the same formulation (ESI; Figure S3): (1) E_{PDMS} is higher, and (2) the limiting stretch (J_{lim}) is lower (Table 1) for all three formulations.(PDMS with comparable nanoparticle concentrations cannot be fabricated due to handling and particle dispersion constraints.) Nanoparticles are well known for producing a stiffening effect on elastomers.[50,51] At the high volume fraction at which they occur around the cavities, the rigid nanoparticles would also decrease the overall stretchability of the PDMS + nanoparticle composite walls (ESI). Employing the assumption that all nanoparticles added to the sample pre-centrifugation locate within the polymerized high internal phase emulsion (polyHIPE), we calculate the enhanced Young's modulus of the cell walls using Mooney's modified version of Einstein's equation[52–54] (ESI) to find an estimate of the Young's modulus of the particulate composite walls, $\tilde{E}_w$ (Table 1). The nearness of the swelling fit modulus to that estimated using Mooney's modification suggests that other effects, such as mechanical constraints due to inter-cavity interactions associated with the complex cellular microstructure (ESI; Figure S4), yield only minor corrections to the fitted material parameters.

Swell stiffening

Given their closely placed liquid compartments separated by thin plate-like structures, PTAs classify as fluid-filled foams. Like other foams, the Young's modulus of fluid-filled foams is less than the modulus of the cell wall material and a function of the structure; e.g., the cell size r_0 and wall thickness t. Unlike typical foams, PTAs are filled with an incompressible fluid. The fluid incompressibility restricts wall deformation to primarily stretching, reducing or eliminating bending and buckling.[55,56] We find that in the absence of turgor pressure (P_t = 0), the modulus of the PTAs generally follows the previous predictions of both Nilsson et al. and Warner et al., who assume linear elastic cell walls of modulus E_w (Figure 3B).[48,49] Using material constitutive parameters obtained from equilibrium swelling, the geometric fit constant for Nilsson et al.'s prediction falls between their predictions for a cubic geometry loaded diagonally and an isodiametric tetrakaidecahedral geometry

with two square faces perpendicular to the direction of applied force. The cells in the PTAs are polyhedral, similar to plant parenchyma cells, suggesting they would be well represented by a tetrakaidecahedron.[49,56,57] We also obtain a constant of order one (2.1) for Warner et al.'s scaling theory indicating reasonable agreement.

Unfortunately, to our knowledge there exists no consensus as to the effect of turgor pressure on the constitutive response of an incompressible fluid-filled (not gas-filled) closed-cell foam.[49,56,58–60] Even the theories by Nilsson et al. and Warner et al.[48] vastly differ in their prediction of the turgor-pressure-dependent response. Nilsson et al. find that the fluid-filled foam composite modulus E_c is linearly proportional to turgor pressure with a constant of proportionality ≈ 3. Warner et al.'s[48] framework (the Warner, Theil, and Donald [WTD] framework) was later adopted to suggest that E_c is independent of turgor pressure for small swelling deformations.[56,61] The latter appears less likely given the predictions of a more complex framework for ideal gas-filled, closed-cell elastomeric foams.[62] That work predicts that increased pore pressure leads to an increase in stiffness.

As Figure 3C shows, we find that PTA modulus is maintained or increases with P_t for all PDMS formulations. To plot this response, we first determine the turgor pressure as a function of the equilibrium swelling. As established in the earlier swelling discussion, at equilibrium, water potential due to osmotic pressure is canceled out by the turgor pressure. Osmotic potential (Ψ_Π) is proportional to the total change in cavity volume,

$$\Psi_\Pi = \Psi_\Pi^0 \frac{V_0}{V}. \qquad \text{(Equation 2)}$$

Thus, at equilibrium, P_t is equal in magnitude to the initial osmotic potential Ψ_Π^0 (given by $\Psi_\pi^0 = -iC_0RT$) divided by the volume expansion ratio at equilibrium V_{eq}/V_0. We observe that the rate of modulus increase with respect to turgor pressure is greatest in all materials at the highest observable turgor pressures. This upturn for all three formulations corresponds to the onset of strain stiffening for the cavity walls (the third point for each formulation in the equilibrium swelling curves shown in Figure 3A). These results suggest nonlinear cell wall behavior plays a role in the stiffness response as well as the swelling response, as found in the previous section. The observation that a modulus increase coincides with strain stiffening is also replicated with a naive adaptation of the WTD framework we report in the ESI. However, this approach is not predictive (Figure S6). Briefly, this approach uses the WTD expression (Figure 3B) to predict E_c after modifying the inputs E_w, r_0, and t from the unstretched state by determining the instantaneous material modulus and geometric changes associated with an expanding thick spherical shell. Together, these findings motivate the need for a turgor-pressure-dependent constitutive model for closed-cell, incompressible fluid-filled elastomeric foams with high pore fraction.

As Figure 4 demonstrates, elastomer PTAs occupy a unique niche in the design space for high-water-content materials exhibiting osmosis-driven deformation. PTAs exhibit two to four times the swelling-induced deformation capabilities observed in plant tissues. Their stiffness is less sensitive to swelling than plants, which may in part be due to a lack of the air pockets typically present in plant tissue,[42,49,57,59,60,63] but is probably due to the opposing nonlinear response of plant cell walls compared with PTA walls. Plant cells strain stiffen at relatively low values of stretch ($1.05-1.1$, corresponding approximately to $V/V_0 \sim 1.16-1.3$).[64,65] At slightly higher swelling, the PTA walls strain soften, further widening the gap illustrated in Figure 4, before the onset of limiting stretch leads them to

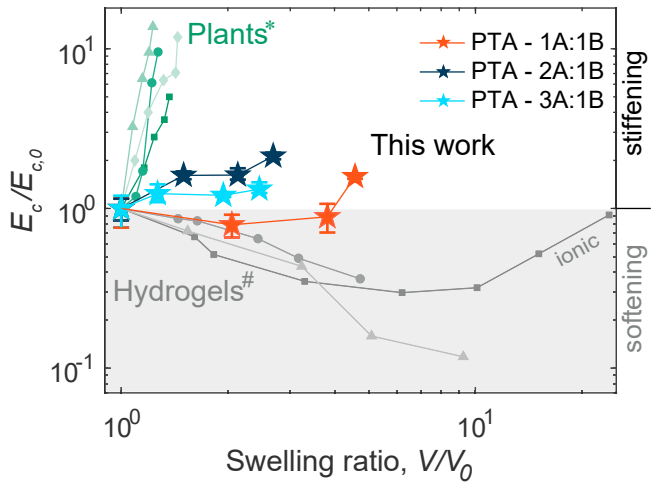

Figure 4. PTAs exhibit an intermediate response between plant tissue and hydrogels

Composite moduli versus swelling response of selected plant tissues (apple, carrot, potato, tomato) are shown in green (data from Lin and Pitt,[42] Georget et al.,[57] and Jackman et al.[63]). PTA results are shown with star symbols. Hydrogels are in gray (data from Sato et al.,[28], Lee et al.,[29] and Dubrovskii.[30]). To facilitate comparison of deformation-induced stiffening, modulus is normalized by its initial value.

increase in stiffness. The magnitude of PTA swelling is similar to that typical of hydrogels, as Figure 4 shows. However, as previously mentioned, hydrogels soften rather than stiffen upon swelling, making them unsuitable for actuation tasks requiring the application of or resistance to high forces.[28–30] To our knowledge, only ionic hydrogels mitigate this effect to some extent, as shown by their non-monotonic swell-stiffening response, which is attributed to finite chain extensibility effects achievable via their initial chain conformation combined with their very high swellability.[30] Despite this impressive behavior, they still only recover the initial modulus, and do not surpass it. Like hydrogels, the PTAs we describe here require only a water potential difference; the continuous phase polymer (silicone in this work) may be readily exchanged to provide the selective permeability desired for a given application environment. Applications such as responsive valves[23] and active biomaterials[66–68] may benefit from such component interchangeability; large, active deformations; and a simultaneous ability to carry or resist load.

Actuation proof-of-concept

Plant tissues are well known for their ability to displace soil and rocks[69,70] or lift themselves against gravity[71,72] by curling or bending.[73] We exploit the fact that PTAs also stiffen upon swelling to mimic similar functionalities. Figures 5A–5E illustrates how a PTA/PDMS bilayer beam (A) curls due to differential swelling (B) to (D), a behavior that is unaffected by the addition of a 5-g weight (E). In contrast, a hydrogel/PDMS beam of similar initial stiffness (Figure 5F) cannot lift the additional weight (I). The deformations of both beams are comparable when unloaded (Figures 5B/5F, 5C/5G, and 5D/5H). In light of recent interest in hydrogels for biomedical soft robots,[24,74] these results suggest that PTAs may provide previously unachievable functionality for soft tissue therapies. Further, PTA's active and high load capabilities are particularly critical in light of recent understanding of the importance of mechanical environment on cell response.[68,75,76]

The bilayer actuators we demonstrate here operate when the PTA or polyacrylamide (PAAm) gel layer swells relative to the PDMS layer that does not, bending

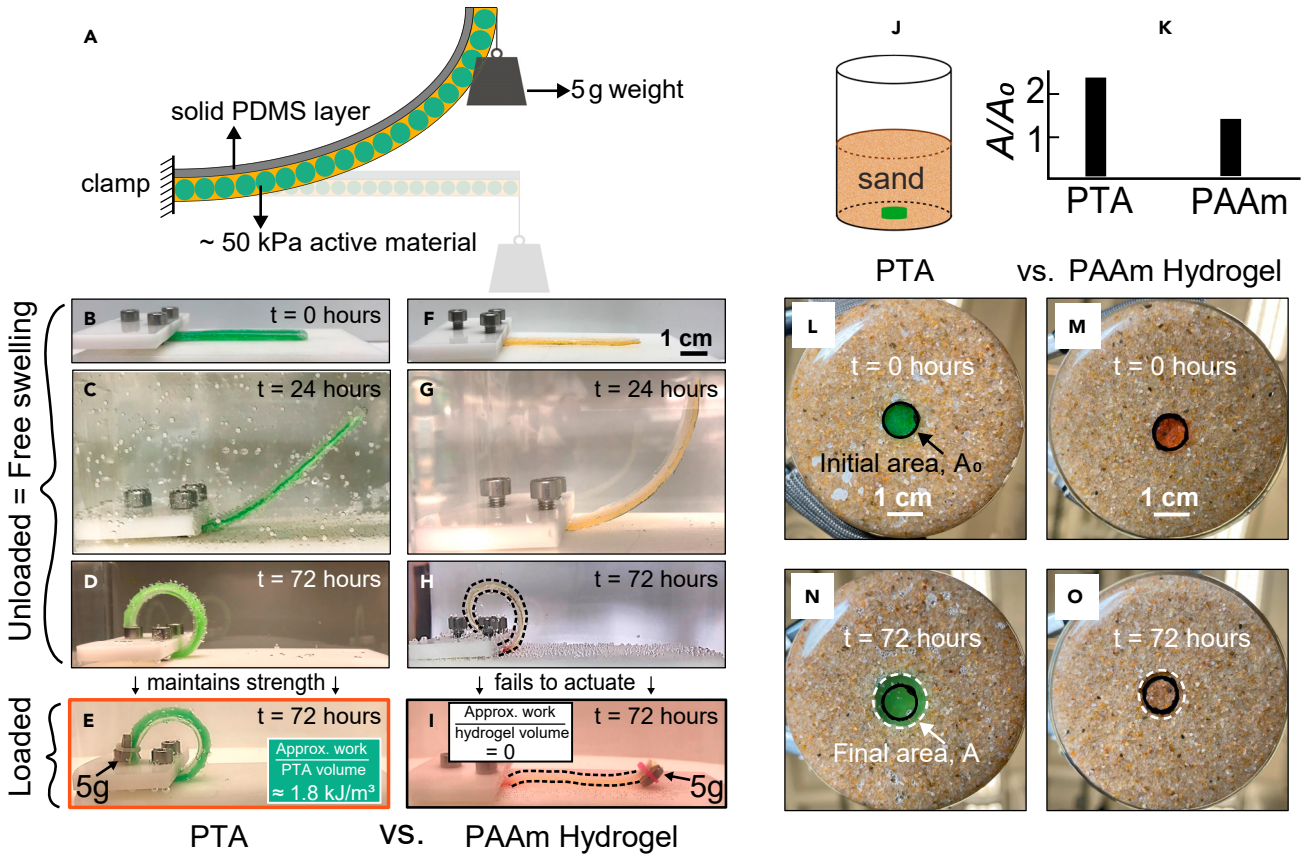

Figure 5. Comparing actuation performance with a typical hydrogel

(A) Schematic of the bilayer bending setup under applied weight. The initial modulus of the active material, either PTA or PAAm hydrogel, is 58 and 49 kPa, respectively.

(B and F) Initial, unloaded test setup photographs for PTA (B), and hydrogel (F) bilayers.

(C–E and G–I) Deformed bilayers 24 h (C and G) and 72 h (D and H)after immersion, respectively, demonstrate identical performance under unloaded conditions. In contrast, (E) and (I) show a stark difference in the final state of bilayers subjected to a 5-g load at the free end, 72 h after immersion. Bilayer performance is estimated as the maximum potential energy of the 5-g weight during actuation normalized by the initial volume of the active material.

(J) A soil dislodgement test demonstrates actuation within confined environments.

(K) The PTA dislodges enough sand to occupy more than twice its originally visible area, $A/A_0>2$.

(L and M) Initial images of the samples through the beaker bottom. Black marker on the glass indicates the initial sample area.

(N and O) PTA and hydrogel after 72 h of swelling. The swollen sample extends outside of the black marker line, as indicated by the white dashed line.

the bilayer in the direction of the PDMS layer (Figure 5A). The hydrogel composition was chosen such that the swelling ratios after 72 h were the same (ESI; Figure S7). Additionally, the initial modulus of the PTA ($E_{PTA}\approx58$ kPa) and hydrogel ($E_{hydrogel}\approx49$ kPa) are very close, giving them similar early swelling force capabilities. During unweighted actuation, the stress within the actuating layer is ~3 kPa in both bilayers according to a modified version of Stoney's formula developed by Cai[77] that is valid even when the gel layer is thicker than the substrate (ESI). In the loaded scenario, the hydrogel is incapable of supporting sufficient stress within the beam, whereas an approximate maximum stress of at least 100 kPa is supported by the PTA according to small deformation composite beam theory. Thus, the PTA produces a force at least 10 times higher than the hydrogel. We anticipate much larger stresses could be accommodated given that the rate of actuation was virtually unaffected by the 5-g load. Leveraging this bilayer concept, PTA actuators can be molded and/or cut into shapes to yield specific motions, such as a soft gripper (ESI; Figure S9).

The PTAs can also operate within confined environments. To penetrate into the ground, plant roots need to apply forces high enough to dislodge soil or obstacles they encounter. Testing similar "pushing" capabilities of the PTAs, we bury 0.15-g discs under 5 cm of sand (Figure 5J). (For faster [but temporary] swelling capacity, we fabricated this PTA with a 33% glycerol solution as the inner phase. We find that, although glycerol provides a larger initial driving force for fluid flow, it is not retained as well by the PDMS membrane and thus leaks out after long periods. PAAm is made to have the same time-dependent unconstrained swelling as the PTA with 33% glycerol solution.) The sand is filled in with water, resulting in a net load of 300 g on the top of the disc, which simultaneously compacts the sand around it. Figures 5L and 5M show images of the discs from beneath the sand immediately upon burial. A black marker line on the bottom of the beaker indicates the initial disc area A_0. After 72 h, the PTA disc more than doubles in area A (Figure 5N), extending outside of the marker line (white dashed line). The PAAm hydrogel disc submitted to the same conditions (Figure 5O) reaches only 56% of the PTA's final area (Figure 5K). It follows that the PTA is capable of applying a much larger force within the confined environment. We observe a similar response for a PTA disc confined within a Styrofoam capsule. The PTA disc breaks open the capsule upon swelling, while a PAAm hydrogel disc simply oozes through the holes in the mesh screen that enabled water flow (Figure S8).

Conclusions

We have demonstrated plant-like, large-deformation, high-water-content, forceful, soft active materials templated from osmotically active elastomeric polyHIPEs. While plants produce large deformations by virtue of growth coupled with osmotic driving forces, PTAs and hydrogels instead overcome an inability to grow through the use of soft polymer networks. Hydrogels soften as they enlarge, but swelling in both non-vascular plant tissue and PTAs is characterized by an ability to apply and/or withstand forces due to their capacity for turgor pressure. Here, we demonstrate PTAs' potential as nastic actuators and closely describe their equilibrium response using a single, fluid-filled, thick-walled, spherical shell consisting of a nonlinear elastic, strain-stiffening solid. Results suggest that finite deformation plays a critical role in modulating the composite stiffness as a function of the turgor pressure within the cells. These findings provide a starting point for designing novel soft active structures using PTAs. Finally, we note that, while the response time of these materials is slow at present, the continuous phase materials used (PDMS) are optimized for mechanical robustness rather than permeability. Increasing the sorption coefficient for water in the wall material (from 10^{-4} to within the range for typical membrane polymers, 0.1) may improve the response time.[6] Nevertheless, in some biomedical applications, a slow response could be desirable to avoid rapid loading of living tissue.

EXPERIMENTAL PROCEDURES

Resource availability

Lead contact

Further information and requests for resources should be directed to and will be fulfilled by the lead contact, Dr. Shelby B. Hutchens (hutchs@illinois.edu).

Materials availability

This study did not generate new unique reagents.

Data and code availability

The authors declare that all data supporting the findings of this study are available within the paper and its supplemental information file. Any additional information

required to re-analyze the data reported in this paper is available from the lead contact upon request.

Fabrication of PTAs

We create PTAs by thermosetting a water-in-PDMS high-internal-phase emulsion as in our earlier work.[40] Colored NaCl solution comprises the aqueous phase. The oil phase is PDMS (Solaris, Smooth On) plus hexane (H-3341, Fisher Scientific). Silica nanoparticles (Aerosil R 974, Evonik Industries) stabilize the emulsion. First, the oil phase and stabilizer (2.8 wt_o% are mixed (1 min; 3,500 rpm; dual asymmetric centrifugal [DAC] mixer, FlackTek), then 23 wt_e% of the aqueous phase is added manually and gently stirred, followed by DAC mixing (12 min). To increase droplet density, the emulsion is centrifuged using a two-step fractionation method. The centrifuged samples are cured at 70°C for 30 min then at room temperature for a day. Changes in PDMS pre-polymer ratio and inner phase viscosity can affect the final cavity size.[40] Table 2 provides the parameters used to ensure that cavity size distribution for materials used in this study remains constant.

PTA swelling test

We incubate a thin disc of PTA ($h = 2$ mm, $d = 10$ mm), cut from a thicker cylindrical sample using a custom slicer, in deionized water at 70° *C* until equilibrium or rupture. Samples are weighed every day for the first 5 days and every other day thereafter. A <5% change in weight for three consecutive readings is taken as equilibrium.

Measurement of elastic modulus of PTAs

We obtain the stiffness[78] of the PTA samples via macro-indentation (Figure S5). Samples are dabbed lightly with Kimwipes (KimTech) and coated with a layer of graphite powder to eliminate adhesion between the sample and the probe. Indentation tests are carried out in a texture analyzer (TA.XT Plus 100, Stable Microsystems) using a 10-mm diameter spherical lens (Edmund Optics) as the probe. Samples are indented to a depth of 0.3 mm at a loading rate of 0.01 mm s^{-1}.

Hydrogel-PDMS bilayer composite fabrication

We dissolve acrylamide (AAm) (Sigma-Aldrich 01700) in deionized water to form a solution of concentration 1.4 m. For every 25 g of water, 0.1 g of N,N′-methylene-bis(acrylamide) (Sigma-Aldrich 146072), 0.25 g of α-ketoglutaric acid (Sigma-Aldrich 75890), 50 μL of 3-(trimethoxysilyl) propyl methacrylate (TMSPMA; Sigma-Aldrich 440159), and 0.05 g of sodium dodecyl sulfate (Sigma-Aldrich L3771) are added as the crosslinker, UV initiator, coupling agent, and surfactant respectively.[79] Food coloring is added to enhance visualization. The solution is poured into a 3D-printed Acrylonitrile Butadiene Styrene mold to a height of 2 mm and UV cured (8 W, 365 nm; 2 cm from the lamp) for 1 h. Fifty microliters of trietoxy(vinyl)silane (TEOVS; Sigma-Aldrich 175560) is added to 10 g of PDMS (Sylgard 184, Dow Corning) precursor mixed in the standard 10:1 (base:curing agent) ratio. The mix is degassed and poured (1-mm thickness) on the cured hydrogel. The PDMS is cured at 70° *C* for 8 h followed by 16 h of room temperature curing. A rectangular bilayer sample (8 cm × 1 cm) is cut using a blade.

PTA-PDMS bilayer composite fabrication

We fabricate a PTA with a 5% glycerol solution as the inner phase and a 1:1 PDMS (Solaris) continuous phase (Table 2). The centrifuged PTA is poured into a polyacrylic mold (8 cm × 1 cm × 3 mm) up to a height of 2 mm. PDMS precursor (Sylgard 184, Dow Corning) mixed in a 10:1 ratio is poured on top of the PTA layer to a thickness of

1 mm. The bilayer is cured at room temperature for 24 h and then extracted from the mold.

SUPPLEMENTAL INFORMATION

Supplemental information can be found online at https://doi.org/10.1016/j.matt.2021.10.015.

ACKNOWLEDGMENTS

This work was supported by the National Science Foundation under grant no. 1653676. The authors thank Elizabeth Slowik and Milena Nutrobkina for their help in determining sample fabrication parameters. Elizabeth Slowik also assisted in performing the tensile tests on Solaris.

AUTHOR CONTRIBUTIONS

A.K. performed the investigation, data curation, and formal analysis. She also created the visualizations and wrote the original draft. S.B.H. conceived the idea, acquired funding, supervised the project, validated the work and its analysis, and reviewed and edited the manuscript.

DECLARATION OF INTERESTS

The authors declare no competing interests.

Received: July 1, 2021
Revised: September 14, 2021
Accepted: October 14, 2021
Published: November 4, 2021

REFERENCES

1. Forterre, Y. (2013). Slow, fast and furious: understanding the physics of plant movements. J. Exp. Bot. *64*, 4745–4760.
2. Braam, J. (2004). In touch: plant responses to mechanical stimuli. New Phytol. *165*, 373–389.
3. Edwards, J., Whitaker, D., Klionsky, S., and Laskowski, M.J. (2005). Botany: a record-breaking pollen catapult. Nature *435*, 164.
4. Martone, P.T., Boller, M., Burgert, I., Dumais, J., Edwards, J., Mach, K., Rowe, N., Rueggeberg, M., Seidel, R., and Speck, T. (2010). Mechanics without muscle: biomechanical inspiration from the plant world. Integr. Comp. Biol. *50*, 888–907.
5. Forterre, Y., Skotheim, J.M., Dumais, J., and Mahadevan, L. (2005). How the Venus flytrap snaps. Nature *433*, 421–425.
6. Geise, G.M., Paul, D.R., and Freeman, B.D. (2014). Fundamental water and salt transport properties of polymeric materials. Prog. Polym. Sci. *39*, 1–42.
7. Wijmans, J.G., and Baker, R.W. (1995). The solution-diffusion model: a review. J. Membr. Sci. *107*, 1–21.
8. Qiu, B., Wang, Y., Fan, S., Liu, J., Jian, S., Qin, Y., Xiao, Z., Tang, X., and Wang, W. (2019). Ethanol mass transfer during pervaporation with PDMS membrane based on solution-diffusion model considering concentration polarization. Separation Purif. Technology *220*, 276–282.
9. Sok, R., Berendsen, H., and Van Gunsteren, W. (1992). Molecular dynamics simulation of the transport of small molecules across a polymer membrane. J. Chem. Phys. *96*, 4699–4704.
10. Watson, J., and Baron, M. (1996). The behaviour of water in poly (dimethylsiloxane). J. Membr. Sci. *110*, 47–57.
11. Biot, M.A. (1941). General theory of three-dimensional consolidation. J. Appl. Phys. *12*, 155–164.
12. Rice, J.R., and Cleary, M.P. (1976). Some basic stress diffusion solutions for fluid-saturated elastic porous media with compressible constituents. Rev. Geophys. *14*, 227–241.
13. Lapsley, K.G., Escher, F.E., Hoehn, E., Lapsley, K.G., and Escher, F.E. (1992). The cellular structure of selected apple varieties. Food Struct. *11*, 6.
14. Barrett, R.M., and Barrett, C.M. (2014). Biomimetic FAA-certifiable, artificial muscle structures for commercial aircraft wings. Smart Mater. Struct. *23*, 074011.
15. Guiducci, L., Weaver, J.C., Bréchet, Y.J.M., Fratzl, P., and Dunlop, J.W.C. (2015). The geometric design and fabrication of actuating cellular structures. Adv. Mater. Inter. *2*, 1500011.
16. Pagitz, M., Lamacchia, E., and Hol, J. (2012). Pressure-actuated cellular structures. Bioinspir. Biomim. *7*, 016007.
17. Luo, Q., and Tong, L. (2013). Adaptive pressure-controlled cellular structures for shape morphing I: design and analysis. Smart Mater. Struct. *22*.
18. Bruhn, B.R., Schroeder, T.B., Li, S., Billeh, Y.N., Wang, K.W., and Mayer, M. (2014). Osmosis-based pressure generation: dynamics and application. PLoS One *9*, e91350.
19. Zhang, H.W., and Lv, J. (2011). Two-scale model for mechanical analysis of nastic materials and structures. J. Intell. Mater. Syst. Struct. *22*.
20. Sinibaldi, E., Argiolas, A., Puleo, G.L., and Mazzolai, B. (2014). Another lesson from plants: the forward osmosis-based actuator. PLoS One *9*, e102461.
21. Freeman, E., and Mauck Weiland, L. (2009). High energy density nastic materials: parameters for tailoring active response. J. Intell. Mater. Syst. Struct. *20*, 233–243.
22. Menges, A., and Reichert, S. (2012). Material capacity: embedded responsiveness. Architectural Des. *82*, 52–59.
23. Beebe, D.J., Moore, J.S., Bauer, J.M., Yu, Q., Liu, R.H., Devadoss, C., and Jo, B.-H. (2000). Functional hydrogel structures for autonomous

flow control inside microfluidic channels. Nature *404*, 588–590.

24. Cangialosi, A., Yoon, C., Liu, J., Huang, Q., Guo, J., Nguyen, T.D., Gracias, D.H., and Schulman, R. (2017). DNA sequence–directed shape change of photopatterned hydrogels via high-degree swelling. Science *357*, 1126–1130.

25. Blacklow, S., Li, J., Freedman, B., Zeidi, M., Chen, C., and Mooney, D. (2019). Bioinspired mechanically active adhesive dressings to accelerate wound closure. Sci. Adv. *5*, eaaw3963.

26. Gong, J.P., Katsuyama, Y., Kurokawa, T., and Osada, Y. (2003). Double-network hydrogels with extremely high mechanical strength. Adv. Mater. *15*, 1155–1158.

27. Sun, J.-Y., Zhao, X., Illeperuma, W.R., Chaudhuri, O., Oh, K.H., Mooney, D.J., Vlassak, J.J., and Suo, Z. (2012). Highly stretchable and tough hydrogels. Nature *489*, 133–136.

28. Sato, K., Nakajima, T., Hisamatsu, T., Nonoyama, T., Kurokawa, T., and Gong, J.P. (2015). Phase-separation-induced anomalous stiffening, toughening, and self-healing of polyacrylamide gels. Adv. Mater. *27*, 6990–6998.

29. Lee, K.Y., Rowley, J.A., Eiselt, P., Moy, E.M., Bouhadir, K.H., and Mooney, D.J. (2000). Controlling mechanical and swelling properties of alginate hydrogels independently by cross-linker type and cross-linking density. Macromolecules *33*, 4291–4294.

30. Dubrovskii, S.A. (1996). Compressional and shear behaviour of weakly ionic polyacrylamide gels. Polym. Gels Networks *4*, 467–480.

31. Kalcioglu, Z.I., Mahmoodian, R., Hu, Y., Suo, Z., and Van Vliet, K.J. (2012). From macro-to microscale poroelastic characterization of polymeric hydrogels via indentation. Soft Matter *8*, 3393–3398.

32. Hu, Y., Zhao, X., Vlassak, J.J., and Suo, Z. (2010). Using indentation to characterize the poroelasticity of gels. Appl. Phys. Lett. *96*, 121904.

33. Yu, Y., Bouklas, N., Landis, C.M., and Huang, R. (2018). A linear poroelastic analysis of time-dependent crack-tip fields in polymer gels. J. Appl. Mech. *85*.

34. Yu, Y., Bouklas, N., Landis, C.M., and Huang, R. (2020). Poroelastic effects on the time-and rate-dependent fracture of polymer gels. J. Appl. Mech. *87*.

35. Sundaresan, V.B., and Leo, D.J. (2006). Protein-based microhydraulic transport for controllable actuation. Smart Struct. Mater. *6168*, 61681S.

36. Su, Y.C., Lin, L., and Pisano, A.P. (2002). A water-powered osmotic microactuator. J. Microelectromechanical Syst. *11*, 736–742.

37. Matthews, L., Sundaresan, V.B., Giurgiutiu, V., and Leo, D.J. (2006). Bioenergetics and mechanical actuation analysis with membrane transport experiments for use in biomimetic nastic structures. Mater. Res. Soc. *21*, 2058–2067.

38. Sinibaldi, E., Puleo, G.L., Mattioli, F., Mattoli, V., Di Michele, F., Beccai, L., Tramacere, F., Mancuso, S., and Mazzolai, B. (2013). Osmotic actuation modelling for innovative biorobotic solutions inspired by the plant kingdom. Bioinspir. Biomim. *8*, 025002.

39. Must, I., Sinibaldi, E., and Mazzolai, B. (2019). A variable-stiffness tendril-like soft robot based on reversible osmotic actuation. Nat. Commun. *10*, 1–8.

40. Kataruka, A., and Hutchens, S.B. (2019). PDMS polymerized high internal phase emulsions (polyHIPEs) with closed-cell, aqueous-filled microcavities. Soft Matter *15*, 9665–9675.

41. Taiz, L., and Zeiger, E. (2002). Plant Physiology, *3* (Sinauer Associates, Inc., Publishers), p. 484.

42. Lin, T.-T., and Pitt, R.E. (1986). Rheology of apple and potato tissue as affected by cell turgor pressure. J. Texture Stud. *17*, 291–313.

43. Wu, H.-I., Spence, R.D., Sharpe, P.J., and Goeschl, J.D. (1985). Cell wall elasticity: I. A critique of the bulk elastic modulus approach and an analysis using polymer elastic principles. Plant Cell Environ. *8*, 563–570.

44. Geitmann, A., and Ortega, J.K. (2009). Mechanics and modeling of plant cell growth. Trends Plant Sci. *14*, 467–478.

45. Van Der Sman, R.G. (2015). Hyperelastic models for hydration of cellular tissue. Soft Matter *11*, 7579–7591.

46. Debotton, G., Bustamante, R., and Dorfmann, A. (2013). Axisymmetric bifurcations of thick spherical shells under inflation and compression. Int. J. Sol. Struct. *50*, 403–413.

47. Gent, A.N. (1999). Elastic instabilities of inflated rubber shells. Rubber Chem. Technol. *72*, 263–268.

48. Warner, M., Thiel, B.L., and Donald, A.M. (2000). The elasticity and failure of fluid-filled cellular solids: theory and experiment. Proc. Natl. Acad. Sci. *97*, 1370–1375.

49. Nilsson, S.B., Hertz, C.H., and Falk, S. (1958). On the relation between turgor pressure and tissue rigidity . II Theoretical calculations on model systems. Physiol. Plant *11*, 818–837.

50. Liu, J., Zong, G., He, L., Zhang, Y., Liu, C., and Wang, L. (2015). Effects of fumed and mesoporous silica nanoparticles on the properties of Sylgard 184 polydimethylsiloxane. Micromachines *6*, 855–864.

51. Azimi, H., Tezel, F.H., and Thibault, J. (2017). Effect of embedded activated carbon nanoparticles on the performance of polydimethylsiloxane (PDMS) membrane for pervaporation separation of butanol. J. Chem. Technol. Biotechnol. *92*, 2901–2911.

52. Fu, S.-Y., Feng, X.-Q., Lauke, B., and Mai, Y.-W. (2008). Effects of particle size, particle/matrix interface adhesion and particle loading on mechanical properties of particulate–polymer composites. Composites B Eng. *39*, 933–961.

53. Mooney, M. (1951). The viscosity of a concentrated suspension of spherical particles. J. Colloid Sci. *6*, 162–170.

54. Einstein, A. (1905). On the movement of small particles suspended in stationary liquids required by the molecular-kinetic theory of heat. Ann. Phys. *4*, 549–560.

55. Warner, M., and Edwards, S.F. (1988). A scaling approach to elasticity and flow in solid foams. Europhys. Lett. *5*, 623–628.

56. Gibson, L.J., Ashby, M.F., and Harley, B.A. (2010). Cellular Materials in Nature and Medicine (Cambridge University Press).

57. Georget, D.M.R., Smith, A.C., and Waldron, K.W. (2003). Modelling of carrot tissue as a fluid-filled foam. J. Mater. Sci. *38*, 1933–1938.

58. Niklas, K.J. (1989). Mechanical behavior of plant tissues as Inferred from the theory of pressurized cellular solids. Am. J. Bot. *76*, 929–937.

59. Pitt, R.E. (1982). Models for the rheology and statistical strength of uniformly stressed vegetative tissue. Trans. ASAE *25*, 1776–1784.

60. Lardner, T., and Pujara, P. (1980). Compression of spherical cells. Mech. Today, 161–176.

61. Gates, R.S., Pitt, R.E., Ruina, A., and Cooke, J.R. (1986). Cell wall elastic constitutive laws and stress-strain behavior of plant vegetative tissue. Biorheology *23*, 453–466.

62. Lopez-Pamies, O., Castañeda, P.P., and Idiart, M.I. (2012). Effects of internal pore pressure on closed-cell elastomeric foams. Int. J. Sol. Structures *49*, 2793–2798.

63. Jackman, R.L., Marangoni, A.G., and Stanley, D.W. (1992). The effects of turgor pressure on puncture and viscoelastic properties of tomato tissue. J. Texture Stud. *23*, 491–505.

64. Zhang, Y., Yu, J., Wang, X., Durachko, D.M., Zhang, S., and Cosgrove, D.J. (2021). Molecular insights into the complex mechanics of plant epidermal cell walls. Science *372*, 706–711.

65. Heyn, A.N. (1933). Further investigations on the mechanism of cell elongation and the properties of the cell wall in connection with elongation. Protoplasma *19*, 78–96.

66. Baker, B.M., Trappmann, B., Wang, W.Y., Sakar, M.S., Kim, I.L., Shenoy, V.B., Burdick, J.A., and Chen, C.S. (2015). Cell-mediated fibre recruitment drives extracellular matrix mechanosensing in engineered fibrillar microenvironments. Nat. Mater. *14*, 1262–1268.

67. Gelmi, A., Cieslar-Pobuda, A., de Muinck, E., Los, M., Rafat, M., and Jager, E.W. (2016). Direct mechanical stimulation of stem cells: a beating electromechanically active scaffold for cardiac tissue engineering. Adv. Healthc. Mater. *5*, 1471–1480.

68. Özkale, B., Sakar, M.S., and Mooney, D.J. (2020). Active Biomaterials for Mechanobiology (Biomaterials), p. 120497.

69. Sadeghi, A., Tonazzini, A., Popova, L., and Mazzolai, B. (2014). A novel growing device inspired by plant root soil penetration behaviors. PLoS One *9*, e90139.

70. Jin, K., Shen, J., Ashton, R.W., Dodd, I.C., Parry, M.A.J., and Whalley, W.R. (2013). How do roots elongate in a structured soil? J. Exp. Bot. *64*, 4761–4777.

71. Hodick, D. (1994). Negative gravitropism in *Chara* protonemata: a model integrating the

opposite gravitropic responses of protonemata and rhizoids. Planta *195*, 43–49.

72. Yamamoto, H., Yoshida, M., and Okuyama, T. (2002). Growth stress controls negative gravitropism in woody plant stems. Planta *216*, 280–292.

73. Holstov, A., Bridgens, B., and Farmer, G. (2015). Hygromorphic materials for sustainable responsive architecture. Constr. Build. Mater. *98*, 570–582.

74. Banerjee, H., Suhail, M., and Ren, H. (2018). Hydrogel actuators and sensors for biomedical soft robots: brief overview with impending challenges. Biomimetics *3*, 15.

75. Discher, D.E., Janmey, P., and Wang, Y.-l. (2005). Tissue cells feel and respond to the stiffness of their substrate. Science *310*, 1139–1143.

76. Yeung, T., Georges, P.C., Flanagan, L.A., Marg, B., Ortiz, M., Funaki, M., Zahir, N., Ming, W., Weaver, V., and Janmey, P.A. (2005). Effects of substrate stiffness on cell morphology, cytoskeletal structure, and adhesion. Cell Motil. Cytoskeleton *60*, 24–34.

77. Cai, S. (2015). Bending a beam by a generalized ideal elastomeric gel. Proc. R. Soc. A. *471*, 20140919.

78. Garcia, M., Schulze, K.D., O'Bryan, C.S., Bhattacharjee, T., Sawyer, W.G., and Angelini, T.E. (2017). Eliminating the surface location from soft matter contact mechanics measurements. Tribol. Mater. Surf. Interfaces *11*, 187–192.

79. Liu, Q., Nian, G., Yang, C., Qu, S., and Suo, Z. (2018). Bonding dissimilar polymer networks in various manufacturing processes. Nat. Commun. *9*, 1–11.